



# A novel high-efficiency visible-light sensitive $\text{Ag}_2\text{CO}_3$ photocatalyst with universal photodegradation performances: Simple synthesis, reaction mechanism and first-principles study

Hongjun Dong<sup>a,b</sup>, Gang Chen<sup>a,\*</sup>, Jingxue Sun<sup>a</sup>, Chunmei Li<sup>a</sup>, Yaoguang Yu<sup>a</sup>, Dahong Chen<sup>a</sup>

<sup>a</sup> Department of Chemistry, Harbin Institute of Technology, Harbin 150001, PR China

<sup>b</sup> Department of Chemistry, Baicheng Normal University, Baicheng 137000, PR China

## ARTICLE INFO

### Article history:

Received 21 September 2012

Received in revised form

27 December 2012

Accepted 30 December 2012

Available online 4 January 2013

### Keywords:

High-efficiency visible-light photocatalyst

Silver carbonate

Universal degradation performance

Theory calculation

Photodegradation mechanism

Photoreaction approach

## ABSTRACT

A novel high-efficiency visible-light sensitive  $\text{Ag}_2\text{CO}_3$  semiconductor photocatalyst was prepared by a simple ion-exchange method based on a strategy incorporating of p-block C element into a narrow bandgap  $\text{Ag}_2\text{O}$ . This photocatalyst exhibits universal high-efficient degradation ability for typically several RhB, MO and MB dyes. Getting insight into degradation patterns of dyes over  $\text{Ag}_2\text{CO}_3$  identifies they are self-oxidation behavior of semiconductor rather than the effect of photosensitization. The reaction mechanism investigated by a series of radical trapping experiments, not only ascertains the major photoreaction approaches of dyes on the surface of  $\text{Ag}_2\text{CO}_3$ , but also reveals the unique universality advantage that arises from selective using one of many activated species to decompose many kinds of dyes such as RhB, MO and MB. The theoretical calculation based on first-principles provides inherently essential evidences for high-efficient oxidation performance of  $\text{Ag}_2\text{CO}_3$  photocatalyst.

© 2013 Elsevier B.V. All rights reserved.

## 1. Introduction

Environmental pollution and energy shortage have become two arduous challenges to the sustainable development of modern human society. Over the past decades, the “Green-life” concept is inspiring enthusiasm to exploit the novel, high-efficient and eco-friendly photocatalysts for air purification and wastewater cleaning [1]. The photocatalytic approach has been broadly investigated and consistently considered as a promising candidate to complement advanced oxidation technologies such as chemical, physical and biological methods [1,2]. Semiconductor photocatalysts have attracted extensive attention because of their potential applications to energy and environmental problems, e.g. water splitting [3,4], carbon dioxide reduction [5], organic contaminant degradation [4,6] and so on. As is well known, the photodegradation of organic pollutants using semiconductor involves photogenerated electrons and holes separating, migrating to the surface of semiconductor, and serving as redox sources that then react with adsorbed organic molecules by a series of complicated redox process, in consequence, giving rise to decomposing organic pollutants.

We emphasize the significance of developing novel visible-light (about 48% of sunlight) sensitive photocatalysts with excellent photodegradation ability and universality for decomposing various organic pollutants. Therefore, the development of the visible-light sensitive photocatalysts for more efficient utilization of the abundant sunlight and indoor light has become one of the desired directions and most important topics in the photocatalytic fields [2–4]. Up to now, more and more studies were carried out for the development of visible-light sensitive photocatalysts, the attempts of which were concentrated on oxides/composite oxides, such as  $\text{TiO}_2$  [6], N-TiO<sub>2</sub> [7], Ag-TiO<sub>2</sub> [8,9], MnO<sub>2</sub> [10], Nb<sub>2</sub>O<sub>5</sub> [11], Fe<sub>3</sub>O<sub>4</sub>/Fe<sub>2</sub>O<sub>3</sub> [12], and sulfides/composite sulfides, such as CdS [13], ZnS [14], MoS<sub>2</sub>/MoS<sub>3</sub> [15], Cu<sub>2</sub>ZnSnS<sub>4</sub> [16]. In recent years, some for Ag-based compounds are believed to be promising high-efficient photocatalysts such as reported silver halides AgX (X=Cl [17–20], Br [21], I [22]), AgInW<sub>2</sub>O<sub>8</sub> [23,24], Ag<sub>2</sub>Mo<sub>3</sub>O<sub>11</sub> [25], AgNb(Ta)O<sub>3</sub> [26], Ag<sub>3</sub>VO<sub>4</sub> [27] and Ag<sub>2</sub>V<sub>4</sub>O<sub>11</sub> [28]. Especially, Ag-based transition metal complex oxide semiconductors, the top of the valence band (VB) of them consist of the unique hybridized Ag 4d and O 2p orbitals, which can lift the top position of the VB and narrow down the bandgap. The bottom of the conduction band (CB) that consists of the relatively delocalized s and/or p orbitals displays significantly dispersity so that it possesses high photogenerated electrons and holes mobility resulting to enhancement of photocatalytic activity of photocatalysts [29]. Moreover, it is also a feasible

\* Corresponding author. Tel.: +86 451 86413753; fax: +86 451 86413753.

E-mail address: [gchen@hit.edu.cn](mailto:gchen@hit.edu.cn) (G. Chen).

and effective designed strategy incorporating p-block elements into a simple narrow bandgap oxide to develop new semiconductor photocatalysts [30]. The reported  $\text{Ag}_2\text{O}$  belongs to a narrow bandgap semiconductor with bandgap of 1.3 eV [31]. Therefore, the incorporation of p-block elements into  $\text{Ag}_2\text{O}$  may broaden the bandgap, enhance oxidative ability, and improve stability of the obtained photocatalyst compared to  $\text{Ag}_2\text{O}$ . At present, a series of successful research works were achieved by this strategy to prepare many new photocatalysts, for instance, the reported  $\text{AgSbO}_3$  [29],  $\text{AgMO}_2$  ( $M = \text{Al}, \text{Ga}, \text{In}$ ) [32–35] and  $\text{Ag}_3\text{PO}_4$  [30,36–40] exhibit high photocatalytic activity under visible-light irradiation.

Herein, in this study, silver carbonate was selected as a novel candidate of visible-light sensitive photocatalyst that prepared by a simple ion-exchange method. The photodegradation patterns and reaction approaches of the methyl orange (MO), methylene blue (MB), and rhodamine B (RhB) dyes over  $\text{Ag}_2\text{CO}_3$  under visible-light with  $\lambda \geq 400$  nm irradiation were investigated in detail. In addition, the theoretical calculation of the energy band dispersion and density of states (DOS) of  $\text{Ag}_2\text{CO}_3$  based on plane-wave-based density functional theory (DFT) was applied to revealing the intrinsically essential evidences of high-efficient photooxidation ability for  $\text{Ag}_2\text{CO}_3$ .

## 2. Experimental

### 2.1. Preparation and characterization of the $\text{Ag}_2\text{CO}_3$ photocatalyst

The  $\text{Ag}_2\text{CO}_3$  samples were prepared by a typically simple ion-exchange method.  $\text{NaHCO}_3$  aqueous solutions ( $0.05 \text{ mol L}^{-1}$ ) were added to the 100 ml  $\text{AgNO}_3$  aqueous solutions ( $0.05 \text{ mol L}^{-1}$ ) drop by drop on ice-water bath conditions until the plenty of yellow green precipitations were generated. The precipitations were washed in turn with secondary distilled water and absolute ethanol to dissolve any unreacted raw materials. Then, the as-prepared  $\text{Ag}_2\text{CO}_3$  products were blow-dried using blower under atmosphere at room temperature. The phase of the as-prepared  $\text{Ag}_2\text{CO}_3$  samples was characterized by powder X-ray diffractometer (XRD, Rigaku D/max-2000) equipped with a  $\text{Cu-K}\alpha$  radiation at a scanning rate of  $5^\circ \text{ min}^{-1}$  in the  $2\theta$  range of  $10$ – $90^\circ$ . X-ray tube voltage and current were set at 45 kV and 50 mA, respectively. The morphologies of the samples were characterized by field-emission scanning electron microscopy (FESEM, FEI QUANTA 200F). X-ray photoelectron spectroscopy (XPS) analysis was measured on an American electronics physical HI5700ESCA system with X-ray photoelectron spectrometer using  $\text{Al K}\alpha$  (1486.6 eV) monochromatic X-ray radiation. The peak positions were corrected against the C 1s peak (285.0 eV) of contaminated carbon. The ultraviolet–visible (UV–vis) diffuse reflectance spectra (DRS) of the samples were recorded on a UV–vis spectrophotometer (PG, TU-1900) at room temperature with  $\text{BaSO}_4$  as the background between 200 and 900 nm. The nitrogen adsorption and desorption isotherm at 77 K was measured using an AUTOSORB-1 Surface Area and Pore Size Analyzer.

### 2.2. Photodegradation properties measurements of the $\text{Ag}_2\text{CO}_3$ photocatalyst

The photodecomposition of the organic dyes was carried out with 0.05 g of the as-prepared  $\text{Ag}_2\text{CO}_3$  powders suspended in the RhB, MO or MB solutions ( $10 \text{ mg L}^{-1}$ , 100 ml) prepared by dissolving the organic dyes powders in distilled water in a quartz glass cell. Then the degradation reaction system was irradiated with a 300W Xe arc lamp (Trusttech PLS-SXE 300, Beijing) equipped with an ultraviolet cutoff filter and/or band pass filter to

provide visible-light with  $\lambda \geq 400$  nm (see Fig. S1, Supporting Information) and/or monochromatic central wavelength visible-light with 550 nm, 420 nm and 475 nm ( $\Delta\lambda = \pm 15$  nm), respectively (see Figs. S2–S4, Supporting Information). Before the suspensions were irradiated, they were carried out under 5 min of ultrasonic process and magnetically stirred for 40 min in the dark to complete the adsorption–desorption equilibrium between dyes and photocatalysts. Lastly, the above suspensions were exposed to the visible-light irradiation under magnetic stirring. UV–vis spectrophotometer (PG, TU-1900) monitored the absorbance of the dyes solutions in degradation process every 5 min. Before measurement, the photocatalysts were removed from the photocatalytic reaction systems by centrifugation.

## 3. Results and discussion

Fig. 1a presents XRD pattern of the as-prepared  $\text{Ag}_2\text{CO}_3$  sample. All the diffraction peaks can be indexed to  $\text{Ag}_2\text{CO}_3$  crystal (JCPDS card No. 70-2184.) with a monoclinic structure, and no diffraction peaks from the impurities are detected. Compared with standard diffraction spectrum, the main diffraction peak at  $2\theta = 33.6^\circ$  corresponding to lattice plane (1 3 0) exhibits the drastic enhancement relative to the others, which indicates that (1 3 0) may be the main exposed and activated lattice plane. Fig. 1b shows the EDS spectrum of the  $\text{Ag}_2\text{CO}_3$  sample that contains C, O and Ag element. The low and high magnified SEM images of the  $\text{Ag}_2\text{CO}_3$  sample in Fig. 1c and d show the obtained products present polyhedral short rod like morphologies with  $1$ – $4 \mu\text{m}$ , homogeneous distributions, and smooth surface, which may be benefit to the dyes absorption and electrons migration on the surface of  $\text{Ag}_2\text{CO}_3$  to improve photocatalytic activity.  $\text{N}_2$  adsorption and desorption isotherms and the Brunauer–Emmett–Teller (BET) specific surface area of the samples was measured (see Fig. S5, Supporting Information). Specific surface area  $0.914 \text{ m}^2 \text{ g}^{-1}$  of  $\text{Ag}_2\text{CO}_3$  was smaller than about  $50 \text{ m}^2 \text{ g}^{-1}$  of  $\text{TiO}_2$  (Degussa P-25). It dedicated that the excellent photodegradation performance was ascribed to ability strong oxidation of  $\text{Ag}_2\text{CO}_3$  instead of the effect of specific surface area. In addition, in an attempt to identify if metal Ag generates or not, the XPS spectra of the  $\text{Ag}_2\text{CO}_3$  sample were investigated to clarify the valance state of each element on the surface of  $\text{Ag}_2\text{CO}_3$ . An XPS survey spectrum obtained from the as-prepared  $\text{Ag}_2\text{CO}_3$  sample is shown in Fig. 2a, which includes Ag 3p, Ag 4d, O 1s, and C 1s peaks. Comparing with the reported O 1s peak of  $\text{Ag}_2\text{O}$  indicates the intensity of the O 1s obtained from  $\text{Ag}_2\text{CO}_3$  is greater than that of  $\text{Ag}_2\text{O}$  [41]. This is expected because the O/Ag ratio in silver carbonate is 1.5, which is greater than that of  $\text{Ag}_2\text{O}$  (0.5). Information regarding the specific nature of these carbon, oxygen and silver species can be gained by examining the high-resolution XPS spectra. Fig. 2b describes the C 1s spectrum of as-prepared  $\text{Ag}_2\text{CO}_3$ . The peaks at 283.5 eV and 288.4 eV are due to carbon in  $\text{Ag}_2\text{CO}_3$  and presence of hydrocarbon contaminants, respectively, which have been observed in the previously reported results assigned to this feature [41]. The peak at 531.0 eV in Fig. 2c is inconsistent with the feature peak of oxygen at 530.2 eV in  $\text{Ag}_2\text{CO}_3$ , which arises from hydroxyl or water species [42]. The reason of stronger peaks of C and O from hydrocarbon contaminants than that from  $\text{Ag}_2\text{CO}_3$  is that, at the present experiments, absolute ethanol used to wash samples may be absorbed on the surface of  $\text{Ag}_2\text{CO}_3$  after blow-dried samples. However, our concern is the XPS spectrum of Ag 3d shown in Fig. 2d consisting of two individual peaks centered at 367.9 eV and 374.0 eV, which are ascribed to the peaks of  $\text{Ag } 3d_{5/2}$  and  $\text{Ag } 3d_{3/2}$  binding energies, respectively. The  $\text{Ag } 3d_{5/2}$  peak of  $\text{Ag}_2\text{CO}_3$  has a shift about 0.3 eV to the lower binding energy compared to the metal Ag  $3d_{5/2}$  peak at 368.2 eV [42], which is opposite to that expected according to simple electronegativity arguments. The anomalous chemical shift for

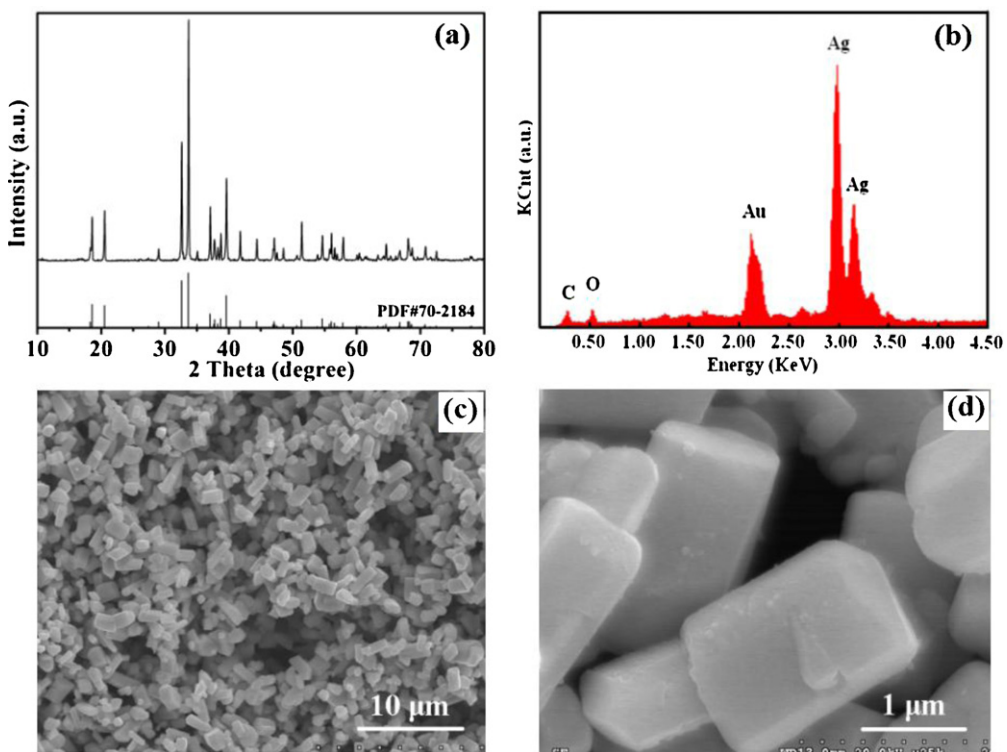


**Fig. 1.** XRD pattern (a), EDS spectrum (b), low magnified SEM images (c), and high magnified SEM images (d) of the  $\text{Ag}_2\text{CO}_3$  samples.

$\text{Ag}_2\text{CO}_3$  is determined by many factors other than electronegativity differences such as lattice potential, work function changes, and extra-atomic relaxation energy. This phenomenon is similar to previously reported  $\text{Ag}_2\text{O}$  [43]. Gaarenstroom and Winograd discussed the influence of extra-atomic relaxation energy on core-level

binding energy shifts of  $\text{Ag}_2\text{O}$  in detail for various cadmium and silver compound [44]. Moreover, the Ag 3d peak becomes broader with a full width at half-maximum (FWHM) from 0.6 eV of metal Ag to 1.7 eV of  $\text{Ag}_2\text{CO}_3$ , which may be due to the presence of the strong interaction between  $\text{Ag}^+$  and  $\text{CO}_3^{2-}$  proved by the calculation result

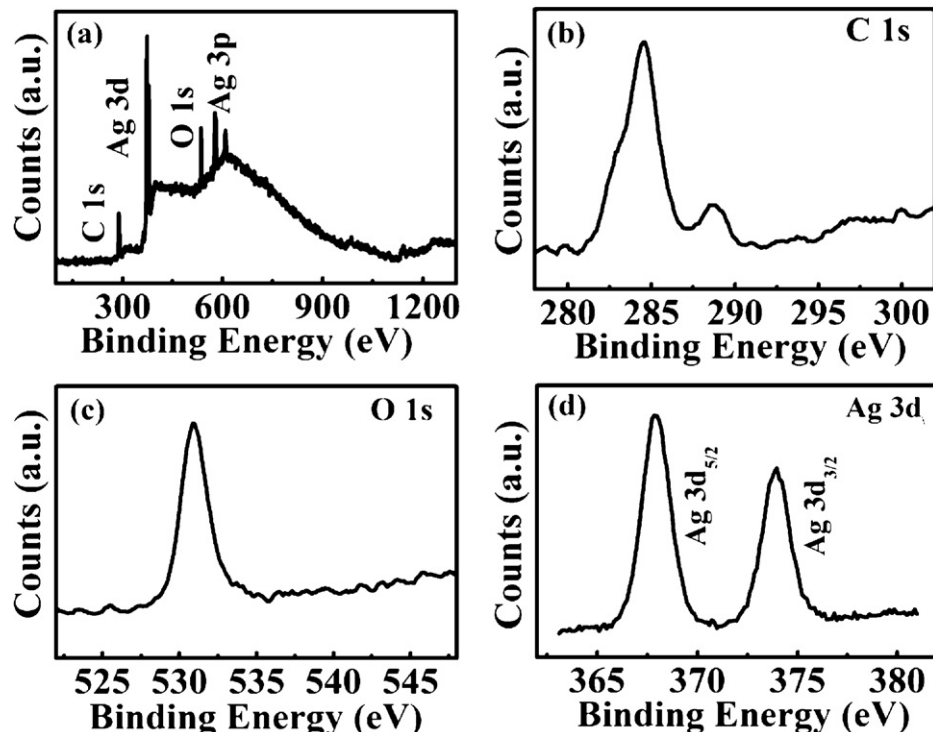


**Fig. 2.** XPS spectra of survey (a), C 1s (b), O 1s (c), and Ag 3d (d) in the  $\text{Ag}_2\text{CO}_3$  samples.

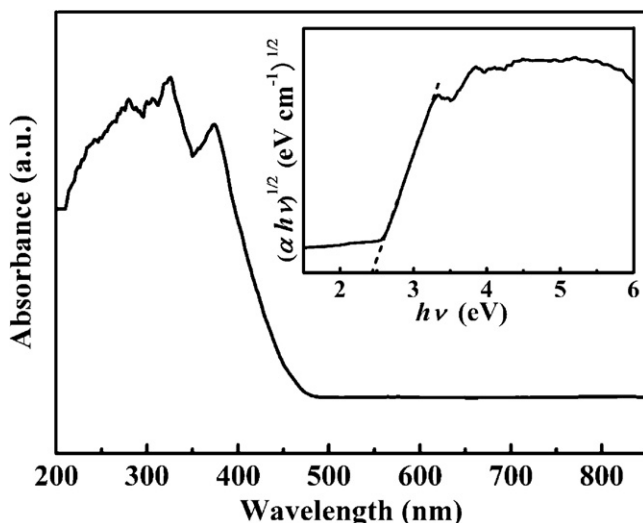


**Fig. 3.** UV-vis diffuse reflectance spectrum and plot of  $(\alpha h\nu)^{1/2}$  versus  $h\nu$  (inset) of the  $\text{Ag}_2\text{CO}_3$  sample.

in Fig. 6c. Therefore, we can confirm no metal Ag generates on the surface of  $\text{Ag}_2\text{CO}_3$ , which is in accordance with the result of XRD analysis.

The optical absorbance of  $\text{Ag}_2\text{CO}_3$  samples was measured by UV-vis diffuses reflectance spectra (DRS). As can be seen from Fig. 3,  $\text{Ag}_2\text{CO}_3$  has an absorption edge around 466 nm and exhibits strong absorption in the visible-light ranges. According to the research method of semiconductor reported by Butler [45], we use the equation  $\alpha h\nu = A(h\nu - E_g)^n$ , where  $\alpha$ ,  $\nu$ ,  $A$ , and  $E_g$  are the absorption coefficient, light frequency, proportionality constant, and bandgap, respectively, and  $n$  value decides type of semiconductor. We define  $\text{Ag}_2\text{CO}_3$  belongs to indirect bandgap semiconductor, which is also demonstrated by theoretical calculation result from Fig. 6a. The bandgap width is estimated to 2.46 eV shown in the insert of Fig. 3. Meanwhile, VB and CB positions are calculated by means of using the empirical formula  $E_{VB} = X - E_e + 0.5E_g$  and  $E_{CB} = E_{VB} - E_g$ , where  $E_{VB}$ ,  $X$ ,  $E_e$ ,  $E_g$  and  $E_{CB}$  are the energy of the VB edge potential, the absolute electronegativity, free electrons on the hydrogen scale (4.5 eV), the bandgap energy and the CB edge potential of the semiconductor, respectively. The top of the VB and the bottom of the CB of  $\text{Ag}_2\text{CO}_3$  are estimated to be 2.75 eV and 0.29 eV (vs. SHE), respectively (see bandgap estimation of  $\text{Ag}_2\text{CO}_3$ , Supporting Information).

In order to study the photodegradation performance of the photocatalyst, the RhB, MB and MO as typical organic pollutants in textile printing wastewater, were used for target molecules to evaluate the degradation ability of  $\text{Ag}_2\text{CO}_3$ . The degradation experiment of three dyes was carried out by their solutions with concentration of  $10 \text{ mg L}^{-1}$  under the visible-light irradiation ( $\lambda \geq 400 \text{ nm}$ ). Fig. 4 shows dynamic curve of MO (a), MB (b) and RhB (c) degradation. We observe the degradation of more than 92% of MO, 97% of MB and 98% of RhB molecules after 15 min, 30 min and 35 min, respectively. Under the same conditions, only 2% of MO, 4% of MB and 7% of RhB were decomposed over the  $\text{TiO}_2$  (Degussa P-25) (see Fig. S6, Supporting Information). It indicates  $\text{Ag}_2\text{CO}_3$  has strong photodegradation ability and a unique universal advantage compared to  $\text{TiO}_2$  (Degussa P-25) for dyes.

Fig. 5a–c shows the absorbance variation of RhB, MB and MO solutions under visible-light at different irradiation time, respectively. The maximum absorption wavelength changes of dyes indicate de-organic-groups are prior to decomposition of benzene/heterocyclic rings [46,47]. However, at the present experiments, the maximum absorption wavelengths of RhB, MB and MO solutions are not shifting, which implies benzene/heterocyclic rings

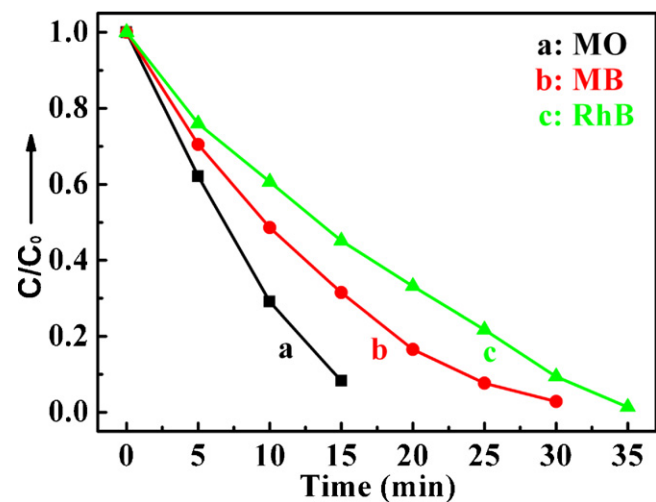


**Fig. 4.** Dynamic curve of MO (a), MB, (b) and RhB (c) degradation over  $\text{Ag}_2\text{CO}_3$  under visible-light with  $\lambda \geq 400 \text{ nm}$ .

are decomposed rather than the simple decoloration process of de-organic-groups [47]. In addition, the absorbance of RhB, MB and MO solutions at ultraviolet regions of 250–380 nm besides visible regions of 400–700 nm are almost disappeared after degradation process, which may indirectly prove the benzene/heterocyclic rings are destroyed, and the organic dye molecules are completely decomposed into small organic/inorganic molecules or/and ions products [48]. The color change photographs of MO, MB and RhB solutions at the degradation process every 5 min are shown in Fig. 5d. All the results as mentioned above demonstrate  $\text{Ag}_2\text{CO}_3$  is a kind of new excellent photocatalysis semiconductor material, which possesses a unique universal advantage to degrade several dyes such as MO, MB and RhB. Furthermore, photocatalytic activity of the photocatalyst is essentially dominated by the energy band structure of the semiconductor, including the positions and compositions of the CB, VB, and the bandgap width. In order to get insight into the high-efficient photooxidation performance of  $\text{Ag}_2\text{CO}_3$ , the bandgap and DOS of  $\text{Ag}_2\text{CO}_3$  and  $\text{Ag}_2\text{O}$  served as comparison were carried out using the plane-wave-based DFT calculation (see calculation method of theory, Supporting Information). Computational bandgaps are 0.80 eV and 0.12 eV for  $\text{Ag}_2\text{CO}_3$  and  $\text{Ag}_2\text{O}$ , respectively, which are lower than experimental values of 2.46 eV and 1.3 eV owing to underestimation of the DFT [49]. In view of explicit analysis for the composition of the top of VB and the bottom of CB, scissor operators of 1.66 eV and 1.18 eV thus were used in bandgap correction. As shown in Fig. 6a, the corrected bandgap dispersion of  $\text{Ag}_2\text{CO}_3$  indicates that  $\text{Ag}_2\text{CO}_3$  belongs to an indirect bandgap semiconductor in line with the experimental result revealed from the absorption spectrum in Fig. 3. Moreover,  $\text{Ag}_2\text{O}$  exhibits direct bandgap semiconductor from corrected bandgap dispersion of  $\text{Ag}_2\text{O}$  in Fig. 6b. The incorporation of p-block Element into  $\text{Ag}_2\text{O}$  directly results to the bandgap broadening of  $\text{Ag}_2\text{CO}_3$ , which can be one significant reason to enhance oxidation ability of  $\text{Ag}_2\text{CO}_3$ . As can be seen from the total DOS and local DOS of  $\text{Ag}_2\text{CO}_3$  in Fig. 6c, the top of VB consisting of the hybridized Ag 4d and O 2p states is similar to that of  $\text{Ag}_2\text{O}$  in Fig. 6d. The bottom of CB is mainly composed of the Ag 5s and Ag 4d states from the local DOS of  $\text{Ag}_2\text{CO}_3$  in the insets of Fig. 6c, but Ag 5s states obviously dominate the bottom of CB. In contrast, the local DOS in the inserts of Fig. 6 displays that the Ag 4d states play a similar status relative to Ag 5s states for the contributions to the bottom of CB of  $\text{Ag}_2\text{O}$ .

$\text{Ag}_2\text{CO}_3$  is well-known ionic compound that is composed of positive  $\text{Ag}^+$  ions and negative  $\text{CO}_3^{2-}$  ionic groups with plane triangle structure. The significant difference of the bottom of CB

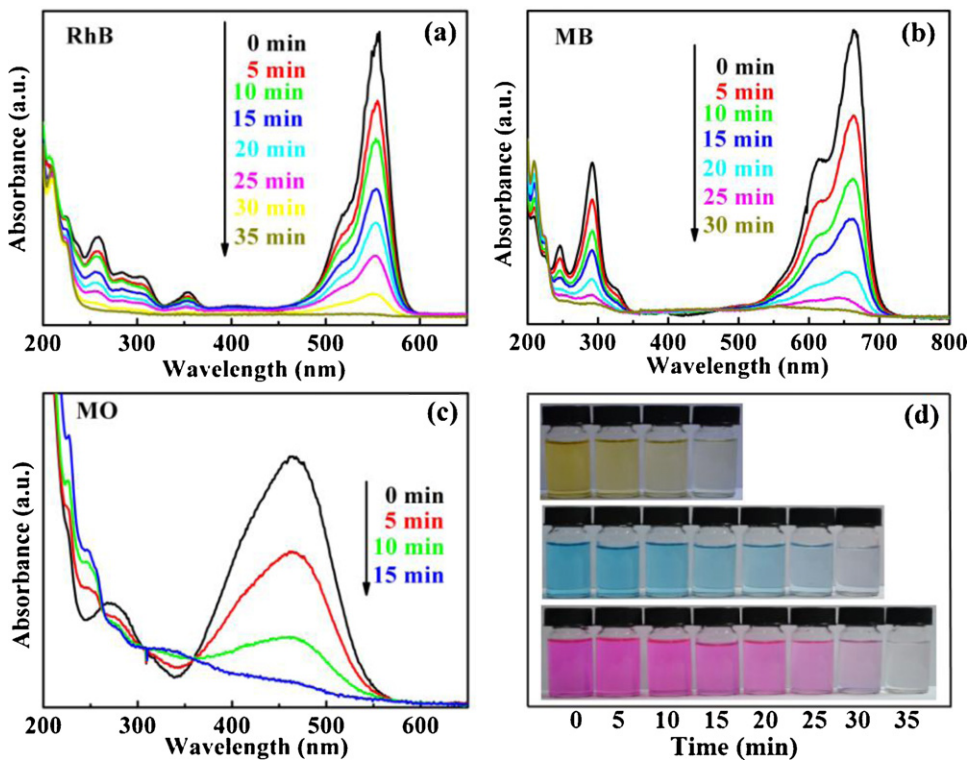


**Fig. 5.** Absorbance variation of RhB (a), MB (b) and MO (c) solutions with  $10 \text{ mg L}^{-1}$  and the color change photographs of MO, MB and RhB solutions at different irradiation time (d).

compositions between  $\text{Ag}_2\text{CO}_3$  and  $\text{Ag}_2\text{O}$  results from the formation of the strongly covalent C—O bonds consisting in  $\text{CO}_3^{2-}$ . As shown in Fig. 6c, the local DOS for O 2s2p and C 2s2p states at approximately  $-9 \text{ eV}$  below the VB are evidenced adequately for bonding states of  $\text{CO}_3^{2-}$ . The partial difference electron density corresponding to one of these bonding states shown in the inserts of Fig. 6c indicates the formation of rigid  $\text{CO}_3^{2-}$  ionic groups with plane triangle structure. The Ag—O bond length of  $\text{Ag}_2\text{CO}_3$  ( $2.3050 \text{ \AA}$ ) greater than that ( $2.0611 \text{ \AA}$ ) of  $\text{Ag}_2\text{O}$  on average

indicates Ag—O bond weaken, and hybridization of Ag 4d and O 2p states is negligible in  $\text{Ag}_2\text{CO}_3$  comparing with that of  $\text{Ag}_2\text{O}$ . It is reflected directly in the local DOS of Ag 4d states in Fig. 6c, where Ag 4d states mainly occupying the top of VB exhibit inconspicuous splitting under  $\text{CO}_3^{2-}$  crystal fields in comparison with that of  $\text{Ag}_2\text{O}$  in Fig. 6d [50]. By contrast,  $\text{Ag}_2\text{O}$  is formed essentially by Ag—O bond, in which Ag 5s and Ag 4d states can form hybridization with O 2p, thus they both appear in the bottom of CB of  $\text{Ag}_2\text{O}$ . It is notable that the shorter distance of Ag—Ag bonds ( $2.8723 \text{ \AA}$ )

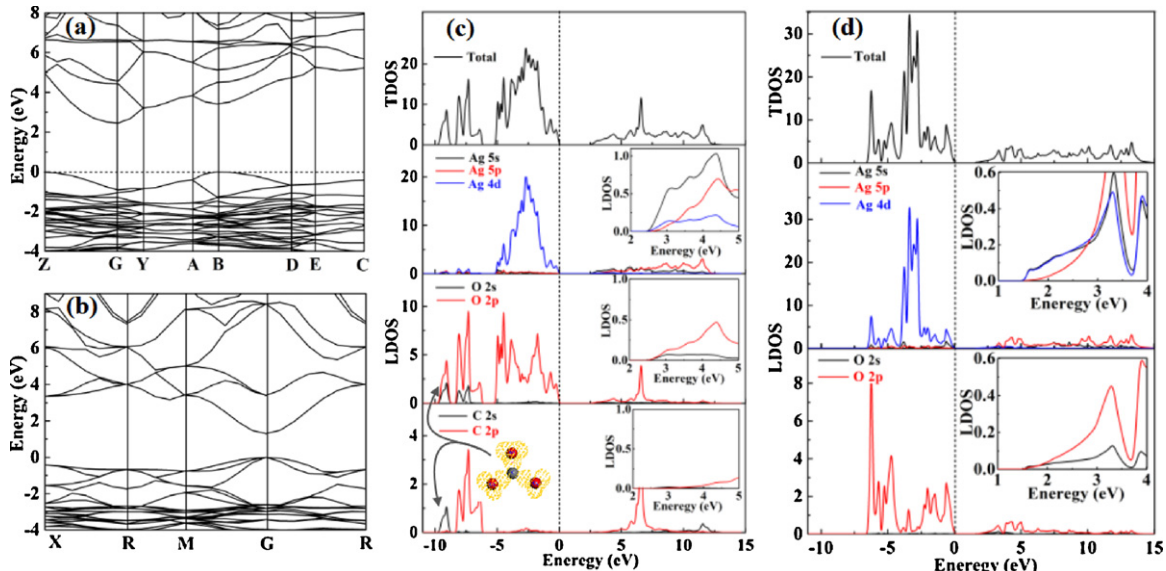


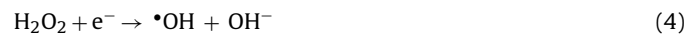
**Fig. 6.** Energy band diagram of  $\text{Ag}_2\text{CO}_3$  (a) and  $\text{Ag}_2\text{O}$  (b), total DOS and local DOS of  $\text{Ag}_2\text{CO}_3$  (c) and  $\text{Ag}_2\text{O}$  (d). The insets of (c) and (d) are extended plots of local DOS near the bottom of CB for  $\text{Ag}_2\text{CO}_3$  and  $\text{Ag}_2\text{O}$ , respectively. The partial difference charge density (e) corresponding to one of the C—O bonding states is shown in the left bottom area in the insert.

in  $\text{Ag}_2\text{CO}_3$  than that in  $\text{Ag}_2\text{O}$  ( $3.3658 \text{ \AA}$ ) manifests between Ag s and Ag s states also takes place hybridization phenomena, resulting in the more dispersive structure of the bottom of CB mainly predominated by Ag s states instead of Ag d states in  $\text{Ag}_2\text{CO}_3$ . The domination of Ag s states is beneficial to the mobility and migration of the photogenerated electrons and holes, which can be the other important reason to improve photocatalytic performance of  $\text{Ag}_2\text{CO}_3$ . In addition, similar to the reported  $\text{Ag}_3\text{PO}_4$  [48], this Ag s–Ag s states hybridization can contribute to decreasing effective mass of the electrons in favor of transferring electrons, which also can be crucial reason to improve photocatalytic performance of photocatalyst.

For the sake of in-depth investigating photodegradation mechanism of dyes, a variety of experiments were performed. The typical experimental method was applied to identify photodegradation patterns including self-oxidation of semiconductor and/or effects of photosensitization [30]. The degradation experiment of RhB over  $\text{Ag}_2\text{CO}_3$  under visible-light with different monochromatic central wavelength irradiation conditions was carried out to ascertain the degradation pattern is self-oxidation behavior of  $\text{Ag}_2\text{CO}_3$  or the possibly evolved effects of photosensitization. It is well known that RhB is mainly excited by a wavelength of approximately 500–580 nm in visible-light regions, whereas  $\text{Ag}_2\text{CO}_3$  can be excited only by a wavelength shorter than 466 nm on account of absorption edge of  $\text{Ag}_2\text{CO}_3$  from UV-vis absorption spectrum in Fig. 3. Therefore, as shown in Fig. 7A(a), monochromatic central wavelength with 550 nm ( $\Delta\lambda = \pm 15 \text{ nm}$ ) visible-light was first used to excite RhB molecules rather than  $\text{Ag}_2\text{CO}_3$ . The result exhibits that RhB molecules are only decomposed less than 5% after 80 min, proving that the effect of photosensitization during degradation processes of RhB molecules over  $\text{Ag}_2\text{CO}_3$  is extraessential and negligible. In contrast, in Fig. 7A(c), monochromatic central wavelength with 420 nm ( $\Delta\lambda = \pm 15 \text{ nm}$ ) visible-light was used to excite  $\text{Ag}_2\text{CO}_3$  instead of RhB molecules. The degradation efficiency of RhB molecules reaches up to approximate 100% after 80 min, which further determines that degradation of RhB is definitely attributed to intrinsically strong photooxidation ability of  $\text{Ag}_2\text{CO}_3$ . Moreover, the same method was performed to investigate degradation pattern of the MO taking advantage of monochromatic central wavelength with 420 nm ( $\Delta\lambda = \pm 15 \text{ nm}$ ) visible-light to only excite  $\text{Ag}_2\text{CO}_3$  and/or monochromatic central wavelength with 475 nm ( $\Delta\lambda = \pm 15 \text{ nm}$ ) visible-light to as much excite MO molecules as possible to prevent excitation of the  $\text{Ag}_2\text{CO}_3$  occurring. The degradation efficiency with 28% of the MO in Fig. 7A(b) increasing to 90% in Fig. 7A(d) after 60 min demonstrates the degradation of MO is mainly also attributed to self-oxidation of  $\text{Ag}_2\text{CO}_3$ . In addition, as shown in Fig. 7A(e), when monochromatic central wavelength with 420 nm ( $\Delta\lambda = \pm 15 \text{ nm}$ ) visible-light exciting  $\text{Ag}_2\text{CO}_3$  was carried out at the degradation process of MB, approximate 100% of MB molecules are decomposed after 70 min, which suggests self-oxidation of  $\text{Ag}_2\text{CO}_3$  plays a major of status in degradation process. Therefore, we can confirm the self-oxidation behavior rather than the effect of photosensitization resulting in degradation of RhB, MO and MB over  $\text{Ag}_2\text{CO}_3$ . Meanwhile, oxidation of semiconductor is closely bound up with generative capacity of different activated species. Therefore, identification of activated species is crucial to confirm the degradation mechanism of the RhB, MO and MB over  $\text{Ag}_2\text{CO}_3$ .

Although photodegradation rate reduction of dyes may relate to the other various factors besides activated species scavengers, it still can serve as a method to research photoreaction approaches of dyes on the surface of photocatalyst, because the interaction between the scavenger and photocatalyst plays a dominant role for impacting on degradation efficiency of dyes. In general, the activated species for photooxidation of dyes mainly include superoxide radicals, hydroxyl radicals and photogenerated holes, while

benzoquinone (BQ) [51,52] and dimethyl sulfoxide (DMSO) [53,54] are well known effective scavengers for  $\cdot\text{O}_2^-$  and  $\cdot\text{OH}$  radicals, respectively. Therefore, in order to get incisive insights into essential of photoreaction mechanism of dyes over  $\text{Ag}_2\text{CO}_3$ , a series of radicals trapping experiments were performed by using of BQ and DMSO scavengers. From the dynamic curves of RhB, MO and MB degradation over  $\text{Ag}_2\text{CO}_3$  under the visible-light in Fig. 7B–D, we observe that both of trapping agents result in, to some extent, suppression of the degradation rate of them, which indicates that  $\cdot\text{O}_2^-$  and  $\cdot\text{OH}$  radicals as oxidation sources generate on the surface of  $\text{Ag}_2\text{CO}_3$ . The possible taking place photoreaction equations are list following:



At the beginning, photogenerated electrons and holes migrate to the surface of  $\text{Ag}_2\text{CO}_3$ . Then photogenerated electrons are captured by dissolved  $\text{O}_2$  in the dyes solutions to produce  $\cdot\text{O}_2^-$  radicals. These  $\cdot\text{O}_2^-$  radicals can directly oxidize dyes or/and immediately react with  $\text{H}^+$  ions to generate  $\text{H}_2\text{O}_2$ , following on converting into  $\cdot\text{OH}$  radicals to oxidize dyes. Simultaneously, photogenerated holes can directly oxidize dyes, as well as react with  $\text{H}_2\text{O}$  and/or  $\text{OH}^-$  ions to produce  $\cdot\text{OH}$ , then oxidizing dyes. However, it should be noticed that the suppressive effects for degradation of RhB, MO and MB exhibit conspicuous difference under the different trapping agents, which signifies  $\cdot\text{O}_2^-$ ,  $\cdot\text{OH}$  radicals and photogenerated holes play different roles in degradation process, thereby, resulting in different degradation approaches of RhB, MO and MB. So, we are able to explore the dominant effect of the above-mentioned activated species based on suppressive degree of degradation rate of them in photoreaction process. In the meantime, we can also ascertain the complicated reactive mechanisms of photoreaction occurring on the surface of  $\text{Ag}_2\text{CO}_3$ . From Fig. 7B(a), the degradation efficiency of RhB decreases significantly from about 100% to 15% when BQ as  $\cdot\text{O}_2^-$  radicals trapping agents is added into the photocatalytic reaction system compared with that of without radicals scavengers in Fig. 7B(c). We conclude the  $\cdot\text{O}_2^-$  radicals are key factors in photooxidation process of RhB, and corresponding photogenerated holes and  $\cdot\text{OH}$  radicals are insignificant. Moreover, the  $\cdot\text{OH}$  radicals are almost not generated by the reaction between photogenerated holes and  $\text{H}_2\text{O}$  and/or  $\text{OH}^-$  in the solutions. In contrast, the degradation efficiency of RhB still reach up to 77% when DMSO as  $\cdot\text{OH}$  radicals trapping agents is present in the reaction systems from Fig. 7B(b). It not only reveals  $\cdot\text{O}_2^-$  radicals play a more important role than  $\cdot\text{OH}$  radicals in oxidation process of RhB owing to the inappreciable oxidation effect of photogenerated holes, but also indicates only small amounts of  $\cdot\text{OH}$  radicals are transformed from  $\cdot\text{O}_2^-$  radicals reacting with photogenerated electrons and  $\text{H}^+$  ions in solutions. So we believe that the major approach for the photodegradation of RhB is oxidation of  $\cdot\text{O}_2^-$  radicals via Eqs. (1) → (2) → (7). Taking the same methods, the degradation efficiency of MO decreases from 92% to 14% when adding BQ in Fig. 7C(a) compared to that with free of radicals scavengers in Fig. 7C(c), which indicates the photogenerated holes are

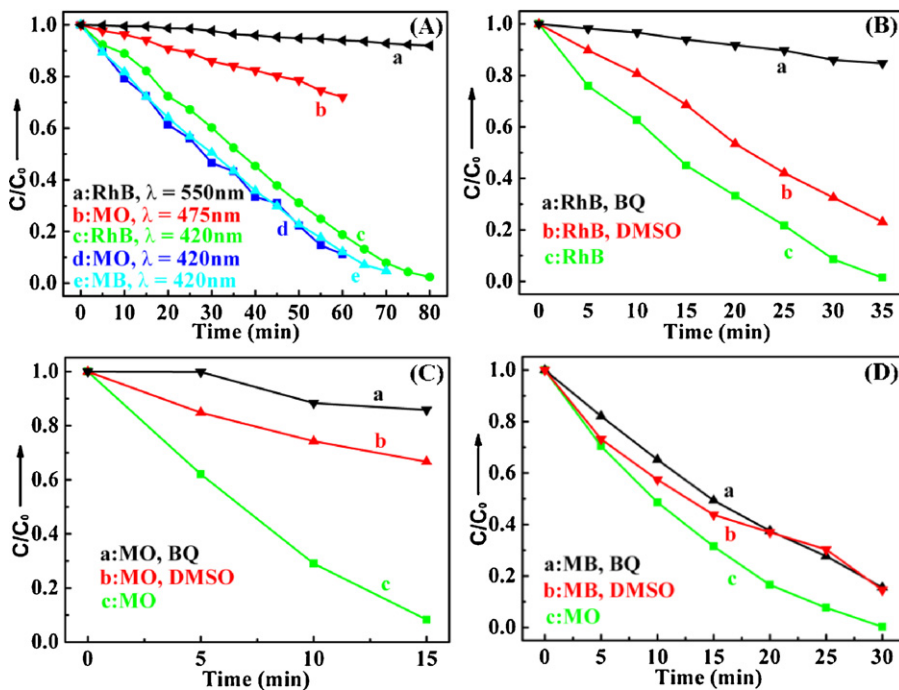


**Fig. 7.** Dynamic curves of RhB, MO, and MB degradation over  $\text{Ag}_2\text{CO}_3$  under visible-light with different monochromatic central wavelength (a) RhB with  $\lambda = 550\text{ nm}$ , (b) MO with  $\lambda = 475\text{ nm}$ , (c) RhB with  $\lambda = 420\text{ nm}$ , (d) MO with  $\lambda = 420\text{ nm}$ , (e) MB with  $\lambda = 420\text{ nm}$ ,  $\Delta\lambda = \pm 15\text{ nm}$  (A). Dynamic curves of RhB (B), MO (C), and MB (D) degradation over  $\text{Ag}_2\text{CO}_3$  added radical scavengers under the visible-light with  $\lambda \geq 400\text{ nm}$  (a: added 3 ml DMSO, b: added  $10^{-4}\text{ mol L}^{-1}$  BQ, c: without radical scavenger).

insignificant for photooxidation of MO, and are not either sources of  $\cdot\text{OH}$  radicals. Meanwhile, after adding DMOS in Fig. 7C(b), the degradation efficiency of MO just reaching to 33% clarifies that  $\cdot\text{OH}$  radicals are more crucial roles than  $\cdot\text{O}_2^-$  radicals owing to transformation of the majority of  $\cdot\text{O}_2^-$  into  $\cdot\text{OH}^-$  radicals. Namely, the major approach for the degradation of MO is oxidation of  $\cdot\text{OH}$  radicals via Eqs. (1)  $\rightarrow$  (2)  $\rightarrow$  (3)  $\rightarrow$  (4)  $\rightarrow$  (9). Fig. 7D(a) shows the degradation efficiency of MB solutions adding BQ is the same as that of solutions adding DMSO in Fig. 7D(b), which still reaches up to 85% compared to that without radicals scavengers in Fig. 7D(c). It proves photogenerated holes are key activated species for degradation of MB, and only a small quantity of  $\cdot\text{O}_2^-$  radicals generate and completely transform into  $\cdot\text{OH}^-$  radicals. We conclude the major approach of the MB degradation is oxidation of photogenerated holes via Eqs. (1)  $\rightarrow$  (8). Fig. 8 shows the band structure schematic

and the possibly occurred photoreaction approaches on the surface of  $\text{Ag}_2\text{CO}_3$ .

It is none other than the various reaction approaches by virtue of selective using one of several activated species, which makes  $\text{Ag}_2\text{CO}_3$  possess a unique universal advantage of decomposing different kinds of dyes. The difference of degradation approaches of these dyes has relations with the interaction between dyes and photocatalysts, which may be determined by the structure characteristic of dye molecules, the absorption site of dye molecules, and the surface activated site of photocatalysts. In general, it is similar to  $\text{TiO}_2$ , both direct bonding [55] and electrostatic interaction [56] are special important interaction modes between the dye and the photocatalyst. As known, the RhB [57], MO [58] and MB molecules display two structures at the equilibrium state in aqueous solutions, respectively, where the left of the equilibrium state is dominant formation that has negative  $\text{R}-\text{CO}_2^-$ ,  $\text{R}-\text{SO}_3^-$  and positive  $\text{R}_2 = \text{N}^+ = \text{R}'$  groups, respectively (see Fig. S7, Supporting Information). On the one hand, the lone pair electron of O atoms in the  $\text{R}-\text{CO}_2^-$  and  $\text{R}-\text{SO}_3^-$  groups can transfer into 4d orbital of the Ag to form a coordination bond, and  $\text{R}_2 = \text{N}^+ = \text{R}'$  groups can also combine with  $\text{CO}_3^{2-}$  groups by electrostatic attraction. On the other hand, the abundantly superficial dangling bonds of Ag and O atoms on the boundary of  $\text{Ag}_2\text{CO}_3$  crystal provide extremely favorable conditions and sites for bonding and/or electrostatic attraction between these dyes and  $\text{Ag}_2\text{CO}_3$ . Hence, RhB and MO molecules selectively connect to Ag atoms, and yet, the MB molecules combine with O atoms of  $\text{CO}_3^{2-}$  on the surface of  $\text{Ag}_2\text{CO}_3$ . In accordance with the DOS of  $\text{Ag}_2\text{CO}_3$  exhibited in Fig. 6c, the bottom of CB and the top of VB are mainly composed of the Ag 5s and Ag 4d states, and the hybridized Ag 4d and O 2p states, respectively. This probably implies that, once  $\text{Ag}_2\text{CO}_3$  samples are exposed to the visible-light, photogenerated electrons transfer to the dominant Ag 5s orbital at the bottom of CB, and photogenerated holes transfer to the hybridized orbital of Ag 4d and O 2p at the top of VB. Consequently, the electrons and holes transport channels are formed around  $\text{Ag}^+$  and  $\text{CO}_3^{2-}$  layers, respectively, which supply the sources of necessary electrons and

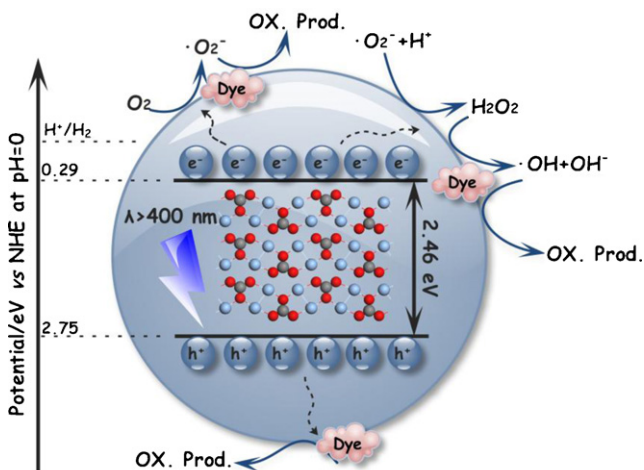


**Fig. 8.** Band structure schematic of  $\text{Ag}_2\text{CO}_3$  and possibly occurring reaction mechanism of dyes on the surface of  $\text{Ag}_2\text{CO}_3$ .

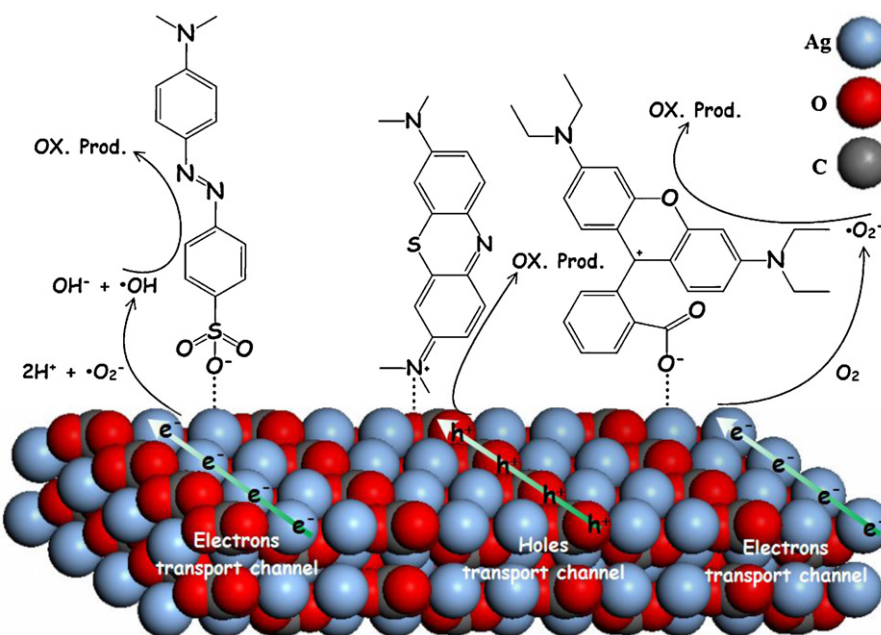


**Fig. 9.** Absorption sites and microreaction schematic of RhB, MO and MB molecules on the (130) lattice plane of  $\text{Ag}_2\text{CO}_3$ .

holes, control type of the activated species generated, and decide degradation approaches of the dyes absorbed on them. We have to mention that the XRD pattern in Fig. 1a manifests (130) lattice plane may be the main exposed and activated lattice plane. It is found that the (130) lattice plane is composed of closely alternative layers of  $\text{Ag}^+$  and  $\text{CO}_3^{2-}$ , which as much as possible exposes Ag and/or O atoms to provide more activated sites and unimpeded photogenerated electrons and holes transport channels. Fig. 9 shows absorption sites and microreaction schematic of RhB, MO and MB molecules on the (130) lattice plane of  $\text{Ag}_2\text{CO}_3$ . When making use of the visible-light irradiation, the photogenerated electrons are immediately trapped by  $\text{O}_2$  to produce  $\cdot\text{O}_2^-$  radicals, then they oxidize RhB molecules connected with superficial Ag atoms at the electrons transport channels. However, the relatively stable azo dye MO molecules connecting with superficial Ag atoms at the electrons transport channels are oxidized by stronger oxidizing  $\cdot\text{OH}^-$  radicals transformed by  $\cdot\text{O}_2^-$  radicals. In contrast, photogenerated holes can directly oxidize MB molecules connected with superficial O atoms located at the holes transport channels. Although all above prove that, as a new high-efficient visible-light sensitive photocatalyst, the universal advantage is our desired result for exploration to the new photocatalyst that can be used in practical application in the future. However, during the cycle experiments, photodegradation ability showed obvious reducing after two times. It indicated the stability of  $\text{Ag}_2\text{CO}_3$  is relatively lower, which was similar to previous works about  $\text{Ag}_2\text{CO}_3$  [59,60]. The similar photocorrosion phenomenon was observed in  $\text{Ag}_3\text{PO}_4$  [40]. Therefore, improving the stability of  $\text{Ag}_2\text{CO}_3$  is still next significant and challenging work.

#### 4. Conclusions

We successfully prepared a new visible-light sensitive  $\text{Ag}_2\text{CO}_3$  semiconductor photocatalyst by a simple ion-exchange method, which exhibits universal high-efficient photodegradation performance for RhB, MB and MO dyes. The theory calculation based on the plane-wave-based DFT indicates the incorporation of p-block C element into narrow bandgap  $\text{Ag}_2\text{O}$  semiconductor broadens the bandgap width and enhances photodegradation ability. The weakening of Ag—O bonds and the occurrence of Ag s—Ag s states

hybridizations render predominance of dispersive Ag s states and reduction of effective electrons mass in the bottom of CB of  $\text{Ag}_2\text{CO}_3$ , which improves the migration and mobility of photogenerated electrons and holes to enhance photocatalytic performance of  $\text{Ag}_2\text{CO}_3$ . Taking use of different monochromatic central wavelength visible-light irradiation method, we definitely confirm the self-oxidation behavior rather than the effect of photosensitization resulting in decomposition of RhB, MB and MO over  $\text{Ag}_2\text{CO}_3$ . A series of radicals trapping experiments using BQ and DMSO scavengers ascertain the discrepant photoreaction approaches of RhB, MB and MO, which attribute to the absorption sites of dye molecules and generated electrons/holes transport channels on the surface of  $\text{Ag}_2\text{CO}_3$ . This unique universal advantage is degrading different kinds of dyes via the various reaction approaches by virtue of selective using one of several activated species.

#### Acknowledgements

This work was financially supported by the National Nature Science Foundation of China (21071036 and 21271055) and Province Natural Science Foundation of Heilongjiang Province (ZD201011). We acknowledge the State Key Laboratory of Urban Water Resource and Environment for the help in characterization.

#### Appendix A. Supplementary data

Supplementary data associated with this article can be found, in the online version, at <http://dx.doi.org/10.1016/j.apcatb.2012.12.041>.

#### References

- [1] Y.F. Li, Z.P. Liu, Journal of the American Chemical Society 133 (2011) 15743–15752.
- [2] J.H. Huang, Y.J. Cui, X.C. Wang, Environmental Science and Technology 44 (2010) 3500–3504.
- [3] J.G. Yu, J. Zhang, S.W. Liu, Journal of Physical Chemistry C 114 (2010) 13642–13649.
- [4] Z.W. Seh, S.H. Liu, M. Low, S.Y. Zhang, Z.L. Liu, A. Mlayah, M.Y. Han, Advanced Materials 24 (2012) 2310–2314.
- [5] J. Lee, D.C. Sorescu, X.Y. Deng, Journal of the American Chemical Society 133 (2011) 10066–10069.

- [6] M. Pelaez, N.T. Nolan, S.C. Pillai, M.K. Seery, P. Falaras, A.G. Kontos, P.S.M. Dunlop, J.W.J. Hamilton, J.A. Byrne, K. O'Shea, M.H. Entezari, D.D. Dionysiou, *Applied Catalysis B: Environmental* 125 (2012) 331–349.
- [7] J.B. Varley, A. Janotti, C.G. Van de Walle, *Advanced Materials* 23 (2011) 2343–2347.
- [8] J.G. Yu, J.F. Xiong, B. Cheng, S.W. Liu, *Applied Catalysis B: Environmental* 60 (2005) 211–221.
- [9] X.M. Zhou, G. Liu, J.G. Yu, W.H. Fan, *Journal of Materials Chemistry* 22 (2012) 21337–21354.
- [10] Y.P. Zhang, Y.L. Yang, Y. Zhang, T.Q. Zhang, M.M. Ye, *Applied Catalysis B: Environmental* 127 (2012) 182–189.
- [11] Y. Zhao, C. Eley, J.P. Hu, J.S. Foord, L. Ye, H.Y. He, S.C. Edman Tsang, *Angewandte Chemie International Edition* 51 (2012) 1–5.
- [12] H.Y. Zhao, Y.J. Wang, Y.B. Wang, T.C. Cao, G.H. Zhao, *Applied Catalysis B: Environmental* 125 (2012) 120–127.
- [13] Q. Li, B.D. Guo, J.G. Yu, J.G. Ran, B.H. Zhang, H.J. Yan, J.R. Gong, *Journal of the American Chemical Society* 133 (2011) 10878–10884.
- [14] Z.G. Chen, L.N. Cheng, H.Y. Xu, J.Z. Liu, J. Zou, T. Sekiguchi, G.Q. Lu (Max), H.M. Cheng, *Advanced Materials* 22 (2010) 2376–2380.
- [15] M.L. Tang, D.C. Grauer, B. Lassalle-Kaiser, V.K. Yachandra, L. Amirav, J.R. Long, J. Yano, A.P. Alivisatos, *Angewandte Chemie International Edition* 50 (2011) 10203–10207.
- [16] A. Singh, H. Geaney, F. Laffir, K.M. Ryan, *Journal of the American Chemical Society* 134 (2012) 2910–2913.
- [17] C.H. An, S. Peng, Y. Sun, *Advanced Materials* 22 (2010) 2570–2574.
- [18] L. Han, P. Wang, C.Z. Zhu, Y.M. Zhai, S.J. Dong, *Nanoscale* 3 (2011) 2931–2935.
- [19] Z.Z. Lou, B.B. Huang, X.Y. Qin, X.Y. Zhang, H.F. Cheng, Y.Y. Liu, S.Y. Wang, J.P. Wang, Y. Dai, *Chemical Communications* 48 (2012) 3488–3490.
- [20] J.G. Yu, G.P. Dai, Huang F.B.B., *Physical Chemistry C* 113 (2009) 16394–16401.
- [21] H.F. Cheng, B.B. Huang, P. Wang, Z.Y. Wang, Z.Z. Lou, J.P. Wang, X.Y. Qin, X.Y. Zhang, Y. Dai, *Chemical Communications* 47 (2011) 7054–7056.
- [22] C. Hu, T.W. Peng, X.X. Hu, Y.L. Nie, X.F. Zhou, J.H. Qu, H. He, *Journal of the American Chemical Society* 132 (2010) 857–862.
- [23] B. Hu, L.H. Wu, S.J. Liu, H.B. Yao, H.Y. Shi, G.P. Li, S.H. Yu, *Chemical Communications* 46 (2010) 2277–2279.
- [24] S.Y. Song, Y. Zhang, Y. Xing, C. Wang, J. Feng, W.D. Shi, G.L. Zheng, H.J. Zhang, *Advanced Functional Materials* 18 (2008) 2328–2334.
- [25] M. Feng, M. Zhang, J.M. Song, X.Gu. Li, S.H. Yu, *ACS Nano* 5 (2011) 6726–6735.
- [26] H. Kato, H. Kobayashi, A. Kudo, *Journal of Physical Chemistry B* 106 (2002) 12441–12447.
- [27] J.M. Song, Y.Z. Lin, H.B. Yao, F.J. Fan, X.G. Li, S.H. Yu, *ACS Nano* 3 (2009) 653–660.
- [28] H.F. Shi, Z.S. Li, J.H. Kou, J.H. Ye, Z.G. Zou, *Journal of Physical Chemistry C* 115 (2011) 145–151.
- [29] T. Kako, N. Kikugawa, J.H. Ye, *Catalysis Today* 131 (2008) 197–202.
- [30] Z.G. Yi, J.H. Ye, N. Kikugawa, T. Kako, S.X. Ouyang, H. Stuart-Williams, H. Yang, J.Y. Cao, W.J. Luo, Z.S. Li, Y. Liu, R.L. Withers, *Nature Materials* 9 (2010) 559–563.
- [31] L.H. Tjeng, M.B.J. Meinders, J. van Elp, J. Ghijsen, G.A. Sawatzky, R.L. Johnson, *Physical Review B* 41 (1990) 3190–3199.
- [32] H. Dong, Z.H. Li, X.M. Xu, Z.X. Ding, L. Wu, X.X. Wang, X.Z. Fu, *Applied Catalysis B: Environmental* 89 (2009) 551–556.
- [33] S.X. Ouyang, H.T. Zhang, D.F. Li, T. Yu, J.H. Ye, Z.G. Zou, *Journal of Physical Chemistry B* 110 (2006) 11677–11682.
- [34] S.X. Ouyang, D. Chen, D.F. Wang, Z.S. Li, J.H. Ye, Z.G. Zou, *Crystal Growth and Design* 10 (2010) 2921–2927.
- [35] S.X. Ouyang, J.H. Ye, *Journal of the American Chemical Society* 133 (2011) 7757–7763.
- [36] Y.P. Bi, S.X. Ouyang, N. Umezawa, J.Y. Cao, J.H. Ye, *Journal of the American Chemical Society* 133 (2011) 6490–6492.
- [37] Y.P. Bi, H.Y. Hu, S.X. Ouyang, G.X. Lu, J.Y. Cao, J.H. Ye, *Chemical Communications* 48 (2012) 3748–3750.
- [38] W. Teng, X.Y. Li, Q.D. Zhao, J.J. Zhao, D.K. Zhang, *Applied Catalysis B: Environmental* 125 (2012) 538–545.
- [39] H.C. Zhang, H. Huang, H. Ming, H.T. Li, LL. Zhang, Y. Liu, Z.H. Kang, *Journal of Materials Chemistry* 22 (2012) 10501–10506.
- [40] G.P. Dai, J.G. Yu, G. Liu, *Journal of Physical Chemistry C* 116 (2012) 15519–15524.
- [41] G.B. Hoflund, J.F. Weaver, W.S. Epling, *Surface Science Spectra* 3 (1994) 157–162.
- [42] J.F. Weaver, G.B. Hoflund, *Chemistry of Materials* 6 (1994) 1693–1699.
- [43] C.Y. Dong, D.S. Shang, L. Shi, J.R. Sun, B.G. Shen, F. Zhuge, R.W. Li, W. Chen, *Applied Physics Letters* 98 (2011) 072107.
- [44] S.W. Gaarenstroom, N. Winograd, *Journal of Chemical Physics* 67 (1977) 3500–3506.
- [45] M.A. Butler, *Journal of Applied Physics* 48 (1977) 1914–1920.
- [46] T.X. Wu, G.M. Liu, J.C. Zhao, *Journal of Physical Chemistry B* 102 (1998) 5845–5851.
- [47] J.D. Zhuang, W.X. Dai, Q.F. Tian, Z.H. Li, L.Y. Xie, J.X. Wang, P. Liu, *Langmuir* 26 (2010) 9686–9694, 26.
- [48] X.X. Hu, C. Hu, *Journal of Solid State Chemistry* 180 (2007) 725–732.
- [49] N. Umezawa, S.X. Ouyang, J.H. Ye, *Physical Review B* 83 (2011) 035202.
- [50] S.X. Ouyang, N. Kikugawa, D. Chen, Z.G. Zou, J.H. Ye, *Journal of Physical Chemistry C* 113 (2009) 1560–1566.
- [51] M. Styliadi, D.I. Kondarides, E.X. Verykios, *Applied Catalysis B: Environmental* 47 (2004) 189–201.
- [52] E. Baciocchi, T.D. Giacco, F. Elisei, F.M. Gerini, M. Guerra, S. Capi, P. Liberali, *Journal of the American Chemical Society* 125 (2003) 16454.
- [53] N.E. Polyakov, T.V. Leshina, E.S. Meteleva, A.V. Dushkin, T.A. Konovalova, L.D. Kispert, *Journal of Physical Chemistry B* 114 (2010) 14200–14204.
- [54] V. Brezova, M. Valko, M. Breza, H. Morris, J. Telser, D. Dvoranova, K. Kaiserova, L. Varecka, M. Mazur, D. Leibfritz, *Journal of Physical Chemistry B* 107 (2003) 2415–2425.
- [55] A. Nawrocka, S. Krawczyk, *Journal of Physical Chemistry C* 12 (2008) 10233–10241.
- [56] K. Bourikas, M. Styliadi, D.I. Kondarides, X.E. Verykios, *Langmuir* 21 (2005) 9222–9230.
- [57] R.W. Ramette, E.B. Sandell, *Journal of the American Chemical Society* 78 (1956) 4872–4878.
- [58] R.G. Sandberg, G.H. Henderson, R.D. White, E.M. Eyring, *Journal of Physical Chemistry* 76 (1972) 4023–4025.
- [59] C.W. Xu, Y.Y. Liu, B.B. Huang, H. Li, X.Y. Qin, X.Y. Zhang, Y. Dai, *Applied Surface Science* 257 (2011) 8732–8736.
- [60] W.G. Wang, B. Cheng, J.G. Yu, G. Liu, W.H. Fan, *Chemistry Asian Journal* 7 (2012) 1902–1908.